

X-ray magnetic circular dichroism and anomalous Hall effect in proton-doped spinel NiCo₂O₄ thin films

M. Wu^{1,*}, Y. Li¹, H. Luo¹, X. Liao¹, W. Liu¹, X. Huang², J. Shi², K. H. L. Zhang^{2,†}, T. Deng¹, Y. Du¹, J. Chen¹, D. Fu¹, H.-Q. Wang¹, and J. Kang¹

¹Engineering Research Center of Micro-nano Optoelectronic Materials and Devices, Ministry of Education; Fujian Key Laboratory of Semiconductor Materials and Applications, CI Center for OSED, and Department of Physics, Xiamen University, Xiamen 361005, People's Republic of China

²State Key Laboratory of Physical Chemistry of Solid Surfaces, College of Chemistry and Chemical Engineering, Xiamen University, Xiamen 361005, People's Republic of China



(Received 27 March 2023; revised 19 May 2023; accepted 8 June 2023; published 21 June 2023)

Element-specified x-ray magnetic circular dichroism (XMCD) and the anomalous Hall effect (AHE) have been investigated to provide deep insights into the magnetic and electronic structural evolutions of different proton-doping spinel NiCo₂O₄ (NCO) films. Our results show that the magnetic dichroism at the Co *L*₂₃-edge is mainly contributed by the spin magnetic moment at the tetrahedral (*T*_d)-site Co²⁺ in pristine NCO. The spin magnetic moments at Co and Ni sites have antiparallel alignments. The magnetic anisotropy is related to the considerable orbital magnetic moments therein. Upon proton-doping in NCO_{int} films (the intermediate state with the mixed phases of H_xNCO and NCO), the magnetic dichroism at the Co *L*₂₃-edge still exists. The doping of one extra electron resides at the octahedral (*O*_h)-site Co³⁺ partially and changes Co³⁺ (*S* = 0) to Co²⁺ (*S* = 3/2). This *O*_h-site Co²⁺ aligns in an antiparallel manner with *T*_d-site Co²⁺ through O-ions mediated antiferromagnetic superexchange interaction, resulting in a reduced spin magnetic moment in NCO_{int} compared to pristine NCO films. Moreover, the reduced magnetic anisotropy in NCO_{int} is due to the decreasing of the orbital magnetic moment, which can be related to the charge redistribution at Co 3*d* energy levels and the crystal-field effect. In the two-proton doped H₂NCO films, the magnetic dichroism is absent where the antiferromagnetism arises from the antiparallel spin alignments of Co²⁺ in *T*_d and *O*_h sites. The intrinsic ferromagnetism is also verified by the AHE, which shows a square-shaped hysteresis as a function of the magnetic fields for pristine NCO and NCO_{int}. Interestingly, the proton-doped NCO_{int} films exhibit an enhanced coercive field and the exchange bias effect with an asymmetric hysteresis loop at low temperatures, which can be ascribed to the antiferromagnetic phase stemming from partial Co valence state reduction by proton doping.

DOI: [10.1103/PhysRevB.107.245128](https://doi.org/10.1103/PhysRevB.107.245128)

I. INTRODUCTION

Electric-field controlled magnetization through an electrolyte-gating approach has attracted considerable research attention recently, realizing effective manipulations of the saturated magnetization [1], coercivity [2], magnetic anisotropy [1,3], exchange bias [4,5], the anomalous Hall effect (AHE) [2], the magnetoresistance effect [2,6], etc. Such manipulations of magnetization, at a small voltage of several volts in a reversible topotactic manner [7], are significant for both a fundamental understanding of the strongly correlated electronic interactions in transition-metal oxides, and for perspective on energy-efficient, high-density data storage in spintronics.

Spinel NiCo₂O₄ (NCO) possesses a high Curie temperature above room temperature, and it has promising applications for developing oxide-bases spintronic devices [8,9]. Motivated by its complex local coordination (tetrahedral:

*T*_d and octahedral: *O*_h), valence states (3+, 2+, and their mixture), spin configurations (high-spin, low-spin, and intermediate-spin), and diverse cation distributions of Ni and Co, NCO is considered as a promising candidate for exploring the electric field controlled multiple functionalities towards practical applications. Wang *et al.* had reported an electric-field controlled metallic ferromagnetic (pristine NCO) to insulating antiferromagnetic (two-proton containing H₂NCO phase) transition through the ionic-liquid gating (ILG) approach at an elevated temperature of 100 °C for 2 h [10]. Recently, we provided the detailed electromagnetic and valence state evolutions in different proton-containing NCO films, where the Ni ions near the Fermi level show the prior Ni³⁺ → Ni²⁺ reduction, and the Co ions exhibit a stepwise Co³⁺ → Co²⁺ [11]. However, a fundamental understanding of the reduced magnetization and the anisotropic field from spin-polarized electronic structure aspects is still lacking. Moreover, spinel NCO epitaxial films have revealed temperature- and thickness-dependent sign reversal of the AHE [8] and topological Hall-effect-like anomalies [12]. The sign change in the AHE can be attributed to the competing effects between impurity scattering and band intrinsic Berry

*m.wu@xmu.edu.cn

†Kelvinzhang@xmu.edu.cn

curvature [8,13], where the Berry phase contribution shows a clear relationship with the metal-insulator transition [14,15]. Studies on the AHE in proton-doped NCO films is required for evaluating the spintronic properties and facilitating its spintronic applications.

In this article, we performed element-specified x-ray magnetic circular dichroism (XMCD) measurements to provide deep insights into the electronic state variations and the specified spin and orbital moments at Co and Ni sites in different proton-doping NCO films. By analyzing the spectral evolutions and quantifying the separated contributions from different T_d - and O_h -coordinated Co and Ni ions on the magnetic dichroism, the origins of magnetism in pristine NCO, NCO_{int} , and H_2NCO have been discussed, where NCO_{int} refers to the intermediate state with the mixed phases of H_xNCO and NCO. Furthermore, the reduced total magnetism in NCO_{int} films has been ascribed to the introduction of one extra electron which resides at O_h -site Co^{3+} , changes the spin configuration of O_h -site Co, and aligns in an antiparallel manner with T_d -site Co^{2+} through O-ion mediated antiferromagnetic superexchange interaction. The reduced magnetic anisotropy is evidenced by the decreasing of the orbital magnetic moment at T_d -site Co^{2+} due to the crystal-field effect. Finally, the AHE is evaluated to verify the intrinsic ferromagnetism, which shows a square-shaped hysteresis as a function of the magnetic fields for pristine NCO and NCO_{int} . The NCO_{int} films exhibit an increased coercive field and the exchange-bias effect that is absent in pristine NCO films, whereas the charge-carrier density remains comparable to that of the pristine NCO films, as discussed in detail below.

II. STRUCTURAL AND MAGNETIC TRANSPORT CHARACTERIZATIONS

High-quality NCO thin films with thickness ~ 40 nm have been deposited on MgAl_2O_4 (100) substrate by PLD at a fixed substrate temperature of 350°C and oxygen partial pressure of 300 mTorr. Previous results show that oxygen partial pressure above 100 mTorr is preferable for retaining the cation distribution close to the stoichiometry [9,14,16–18]. With the above deposition conditions, the NCO pristine films show a metallic ferromagnetic ground state with a saturated magnetization of $\sim 2 \mu_B/\text{f.u.}$, suggesting that the cations distribute close to the ideal stoichiometry. Afterwards, NCO films have been treated with the ILG method, as in the schematic view shown in Fig. 1(a). By applying a positive bias, the protons can be incorporated into NCO films. In response to the structural expansion and the doping of one additional electron, the physical properties of NCO films change dramatically. However, the proton incorporation in NCO film is a stepwise procedure. Details of the structural, electromagnetic, and valence state variations have been reported recently [11]. We focus here on H_xNCO films at three representative stages, i.e., the pristine NCO with $x = 0$, the intermediate state NCO_{int} with mixed phases [with H_xNCO ($0 < x < 2$) as the upper layer and NCO as the lower layer] at treatment conditions as (+3 V, RT, 30 min), and the protonated film with $x = 2$ [i.e., H_2NCO at treatment conditions as (+3 V, 100°C , 2 h)]. Figure 1(c) exhibits the normalized hydrogen depth profiles in pristine NCO, NCO_{int} , and H_2NCO , respectively.

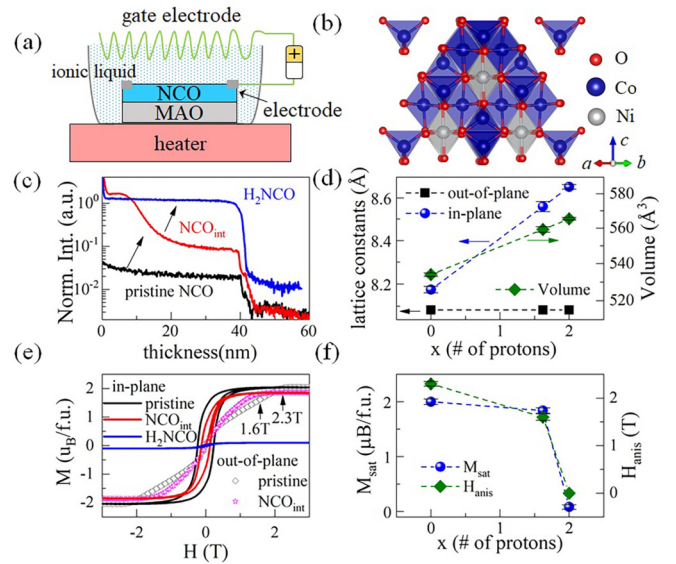


FIG. 1. (a) Schematic illustration of the ILG experimental setup. (b) Illustration of the inverse spinel structure of NCO. (c) The depth profiles of normalized hydrogen intensity ratios in the investigated NCO films. (d) Lattice parameters and unit-cell volume at different x values in H_xNCO assuming a linear hydrogen concentration and volume expansion relationship. (e) The MH hysteresis loops for pristine NCO and NCO_{int} films along in-plane and out-of-plane directions. (f) The saturated magnetic moment M_{sat} and the anisotropy magnetic field H_{anis} at different x values. The in-plane and out-of-plane lattice parameters in the figures were adopted from Ref. [11].

The hydrogen depth profiles have been obtained through the high-resolution time-of-flight secondary-ion mass spectrometry (TOF-SIMS) technique, as shown in Ref. [11]. Our TOF-SIMS data suggest that the proton doping is a stepwise procedure. Compared to pristine NCO, the fully protonated H_2NCO film shows approximately two orders of magnitude higher hydrogen intensity accompanied by a homogeneous hydrogen distribution. For the NCO_{int} , the hydrogen ions accumulate at the surface region with a depth extension of approximately one-third of the total thickness. Therefore, the proton doping in NCO_{int} film is inhomogeneous, which changes the magnetic states and induces the exchange-bias effect therein, as will be discussed in detail below.

Figure 1(d) exhibits the in-plane (a) and the out-of-plane (c) lattice parameters at different x values. All films are fully strained to the substrate with the same in-plane lattice constant ($a = 8.083 \text{ \AA}$) as that of the MAO substrate, as suggested by the reciprocal space maps in our previous work [11]. The out-of-plane lattice constant values increase substantially as proton incorporation. We note that previous studies show a clear correlation between hydrogen concentration and the volume expansion in transition-metal oxides [19,20]. Accordingly, we can estimate the hydrogen content in NCO_{int} from its crystalline volume assuming a linear dependence, which is $\sim (1.55 \pm 0.8)$ as shown in Fig. 1(d). Figure 1(e) shows the magnetic hysteresis (MH) loops along in-plane and out-of-plane directions for the investigated NCO films. Figure 1(f) summarizes the variations of magnetic properties, i.e., the saturated magnetic moment M_{sat} , and the anisotropy

magnetic field H_{anis} at which value the perpendicular magnetic anisotropy vanishes. Briefly, NCO pristine film shows saturated $M_{\text{sat}} \sim 2 \mu_B/\text{f.u.}$ and $H_{\text{anis}} \sim 2.3$ T. With an increase in x , both the M_{sat} and H_{anis} values decrease, which eventually change to approximately zero for H_2NCO with an antiferromagnetic ground state.

To provide deep insights into the magnetic evolutions and their origins from a spin-polarized electronic structure point of view, we performed element-specific XMCD measurements of NCO films at three representative stages. The measurements were performed at the Magnetic Circular Dichroism beamline (BL12B) of National Synchrotron Radiation Laboratory (NSRL) and the BL08U1-A beamline at Shanghai Synchrotron Radiation Facility (SSRF). We note that the datasets are reproducible for different samples. The XMCD data were collected in the total electron yield mode by changing the helicity of the incoming x-ray beam while keeping the moments aligned in the same direction. The experiments were performed with an applied magnetic field of 9 T at a temperature of 5 K. The sample is 30° tilted with respect to the incoming beam during the measurements. Furthermore, temperature- and magnetic-field-dependent Hall measurements have been performed in a van der Pauw geometry for pristine NCO and NCO_{int} with ferromagnetic ground states to verify the intrinsic spin-polarized charge carriers and their features.

III. RESULTS AND DISCUSSIONS

A. XMCD measurements

Figures 2(a) and 2(b) show the experimental measured XAS spectra at the $\text{Co } L_{23}$ -edge and the $\text{Ni } L_{23}$ -edge with different circular right and circular left polarizations of pristine NCO, NCO_{int} , and H_2NCO films, respectively. Apparently, the XAS spectra measured at different circularly polarized beam are distinct. In the ideal case, NCO with an inverse spinel structure has a specified chemical formula as $[\text{Co}^{3+}]_{T_d}[\text{Ni}^{2+}\text{Co}^{3+}]_{O_h}\text{O}_4$ [9,16,17]. However, previous results show that some of the T_d Co^{3+} ions can be Co^{2+} practically, which drives the O_h Ni^{2+} to Ni^{3+} for charge conservation. The coordination formula can be expressive as $[\text{Co}_{1-\delta}^{3+}\text{Co}_\delta^{2+}]_{T_d}[\text{Ni}_{1-\delta}^{2+}\text{Ni}_\delta^{3+}\text{Co}^{3+}]_{O_h}\text{O}_4$ [21,22]. Previously, we had performed detailed investigations on the local cation distribution in pristine NCO thin films with an identical setup and deposition conditions. Based on a combination of XAS and configuration interaction cluster calculations, our results showed that the averaged valence states are $\text{Ni}^{2.5+}$ and $\text{Co}^{2.6+}$ in pristine NCO films, corresponding to $\delta \approx 0.5$ therein [9,11]. We further note that this $\delta \approx 0.5$ is consistent with the results presented by Bitla *et al.* in ferrimagnetic NCO films using XAS and XMCD spectra as fingerprints [23].

For pristine NCO film, $\text{Co } L_{23}$ -edge XAS spectra indeed reveal the mixed Co^{2+} and Co^{3+} valence states denoted as peaks a and b in Fig. 2(a), which can be associated with Co^{2+} and Co^{3+} in both O_h and T_d coordination, respectively. The magnetic dichroism is mainly contributed by peak a , which can be assigned to Co^{2+} with T_d coordination. In other words, the magnetic signal is dominantly contributed by the spin magnetic moment in the T_d -site Co^{2+} , rather than the O_h -site

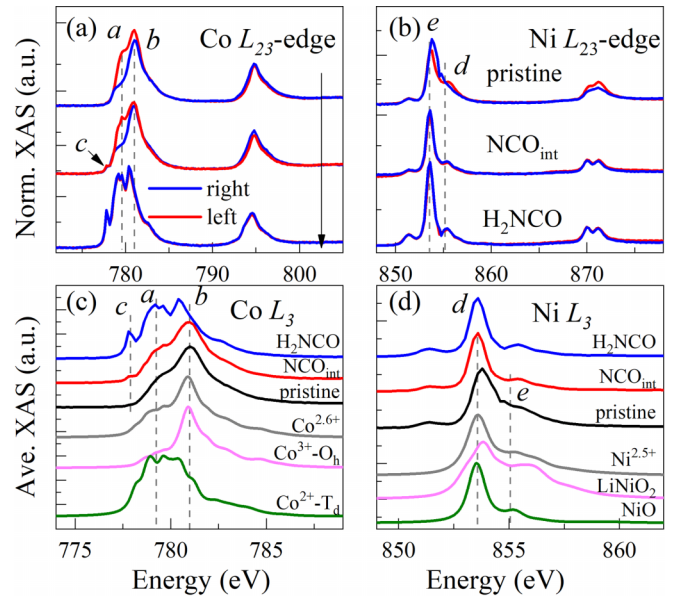


FIG. 2. (a),(b) Normalized XAS spectra at $\text{Co } L_{23}$ -edge and $\text{Ni } L_{23}$ -edge measured with different circular-polarized helicities for pristine NCO, NCO_{int} , and H_2NCO films, respectively. (c),(d) Corresponding averaged XAS spectra at $\text{Co } L_3$ edge ($\text{Ni } L_3$ edge) for H_2NCO , NCO_{int} , pristine NCO, the mixed $\text{Co}^{2.6+}$ absorption spectra obtained by linear combination of T_d -site Co^{2+} (ZnCo_2O_4) and O_h -site Co^{3+} (CoAl_2O_4), as well as $\text{Ni}^{2.5+}$ absorption spectra obtained by linear combination of O_h -site Ni^{2+} (NiO) and Ni^{3+} (LiNiO_2), respectively. The spectra are shifted vertically for clarity.

Co^{3+} valence state. However, small magnetic dichroism has also been resolved from peak b . Given that the O_h -site Co^{3+} ($3d^6: t_{2g}^6 e_g^0$) has $S = 0$ in the low-spin configuration, it should have no contribution to the magnetic signal. The magnetic dichroism from peak b is expected to be related to T_d -site Co^{3+} .

Upon protonation, two features have been observed. The magnetic dichroism at peak b decreases, implying that partial T_d - Co^{3+} is reduced to Co^{2+} . Moreover, additional peak c appears. The prepeak structure of peak c denotes the Co^{2+} surrounded by O ions with O_h coordination. In the one-electron picture of O_h -site Co^{2+} , the first excitation peak c corresponds to the transfer from $2p$ core level to the lowest empty state of t_{2g} orbital, similar to what was observed in CoO with the same $\text{Co}^{2+} 3d^7$ electronic configuration [24]. In terms of the valence state variations of Co^{3+} upon protonation with the addition of one electron, the changes of $\text{Co } L_{23}$ -edge XAS spectra imply that both T_d - Co^{3+} and O_h - Co^{3+} are reduced to Co^{2+} partially. This is consistent with the comparable on-site energies of Co^{3+} in different O_h and T_d coordination as suggested by density functional theory calculations [9,11]. With full protonation, a distinct shift of peak positions towards Co^{2+} and changes of the spectral line shape have been observed. The protonated H_2NCO is dominated by the Co^{2+} valence state, whereas the magnetic dichroism is absent due to the antiparallel spin alignments of Co^{2+} in T_d and O_h sites, respectively.

Figure 2(c) shows the averaged XAS (by averaging the circular left- and right-polarized XAS spectra, and normalized

to the peak value at L_3 edge) spectra at the Co L_3 edge. Using the experimentally measured XAS spectra from spinel ZnCo_2O_4 (Co^{2+} , $3d^7$ electronic configuration and T_d coordination) and CoAl_2O_4 (Co^{3+} , $3d^6$ electronic configuration and O_h coordination) as references, the NCO pristine films exhibit the mixed valence state as $\text{Co}^{+2.6}$, as suggested by combined XAS and configuration-interaction cluster calculations [9]. Moreover, the Co valence state variation exhibits a gradual $\text{Co}^{3+} \rightarrow \text{Co}^{2+}$ evolution. From the variation of the magnetic dichroism between circular left and right polarized x-rays, we further ascertain that the valence state variations happen partially at both T_d - Co^{3+} and O_h -site Co^{3+} .

Regarding Ni L_{23} -edge XAS spectra at different circularly polarized x-rays, the main changes exist in peaks d and e at the Ni L_3 -edge as shown in Fig. 2(b). Peak d is located at a comparable energy position to Ni^{2+} . However, for pristine NCO film, instead of single peak d as shown in protonated NCO films, a broadening of peak d has been resolved with the peak weight center shifting towards higher energies. This implies a considerable Ni^{3+} contribution. We note that the Ni L_3 peak in NCO pristine film is distinct from individual Ni^{2+} and Ni^{3+} with specified spectral weight contributions. Figure 2(d) shows the XAS spectrum of $\text{Ni}^{+2.5}$ known as the identified oxidation state in stoichiometry NCO films obtained from different experimental approaches [9,18], using experimentally measured LiNiO_2 (Ni^{3+} , $3d^7$) and NiO (Ni^{2+} , $3d^6$) with O_h coordination. The linearly combined Ni L_{23} -edge absorption spectrum is clearly different from that of pristine NCO films, where the Ni^{3+} and Ni^{2+} absorption peaks are smeared out in the latter case. This implies that Ni is preferred as the intermediate valence state between Ni^{3+} and Ni^{2+} , which can be valid for nickel oxides due to the strong Ni $3d$ - O $2p$ hybridization where the ground-state wave function has a considerable contribution from oxygen ligands [25,26]. Moreover, the magnetic dichroism has only been observed for pristine NCO film. Upon protonation, Ni changes to Ni^{2+} valence state without magnetic signals, indicating Ni^{2+} as the low-spin configuration ($S = 0$). Therefore, our results suggest that the magnetism in pristine NCO is mainly contributed by T_d -site Co^{2+} and O_h -site $\text{Ni}^{2.5+}$, whereas the ferromagnetic signal in NCO_{int} is contributed by T_d -site Co^{2+} after compensating the antiparallel spin alignments at O_h -site Co^{2+} .

B. XMCD sum-rule analyses

To further evaluate the spin and orbital magnetic moment at Co and Ni sites quantitatively, we performed XMCD sum-rule analyses. The sum-rule equations for the $2p \rightarrow 3d$ dipole transition are given by [27]

$$2\langle S_z \rangle + 6\langle T_z \rangle = \left(\frac{5p - 3q}{r} \right) N_h, \quad \langle L_z \rangle = \left(\frac{2q}{r} \right) N_h, \quad (1)$$

where $\langle S_z \rangle$, $\langle L_z \rangle$, and $\langle T_z \rangle$ are the expectation values of the spin magnetic moment, orbital magnetic moment, and magnetic dipole moment, respectively. We note that the expectation value of spin moment $\langle S_z \rangle$ is evaluated by assuming that $\langle T_z \rangle$ is negligible due to the cubic symmetry of the $3d$ orbitals [27]. Moreover, p and q correspond to the integrated intensity values of the XMCD spectrum at L_3 and L_2 postedges, respectively. The parameter r refers to the integrated XAS

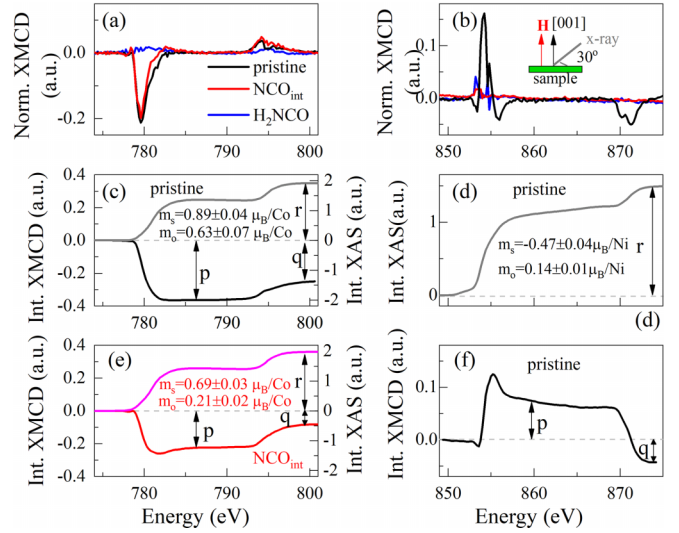


FIG. 3. The normalized XMCD signal (a),(b) and the integrated XAS, XMCD intensities (c)–(f) at Co L_{23} -edge and Ni L_{23} -edge for pristine NCO and NCO_{int} films, respectively. The inset of panel (b) shows the XMCD measurement geometry. The spin and orbital magnetic moments are shown in the corresponding spectra.

intensity value after subtracting the step function at Co and Ni L_{23} -edge, as labeled in Fig. 3. N_h is the number of holes of the corresponding ion.

Figure 3 shows the normalized XMCD spectra and the integrated XAS, XMCD intensities for different samples. The inset of panel (b) shows the schematic view of the measurement geometry. First, opposite XMCD signals have been revealed at Co and Ni L_{23} -edge, indicating that the spin magnetic moments of Co and Ni are aligned in an antiparallel manner. Accompanying the gradual valence state variation at the Co L_{23} -edge, the XMCD signals also decrease simultaneously. For pristine NCO film, the spin magnetic moment is $\sim(0.89 \pm 0.04) \mu_B/\text{Co}$ assuming the number of holes $N_h = 3$ (corresponding to Co^{2+} with $3d^7$ electronic configuration). The corresponding orbital moment is evaluated as $\sim(0.63 \pm 0.07) \mu_B/\text{Co}$. Orbital moment quenching has been proven for some $3d$ ions, whereas for $3d^6$ and $3d^7$ electronic configurations, the orbital moment is only partially quenched due to the symmetry being broken even in a cubic crystal field. Moreover, this considerable orbital magnetic moment is the decisive factor for the perpendicular magnetic anisotropy. Upon protonation, the spin and orbital magnetic moments decrease as shown in Fig. 3(e). The spin and orbital magnetic moments are calculated as $\sim(0.69 \pm 0.03) \mu_B/\text{Co}$ and $\sim(0.21 \pm 0.02) \mu_B/\text{Co}$ for NCO_{int} , respectively. The total magnetization is decreased, which agrees well with the reduction of saturated magnetization as resolved in an MH hysteresis loop compared to pristine NCO. Furthermore, the anisotropy field representing the perpendicular magnetic anisotropy decreases from ~ 2.3 T to ~ 1.6 T, which can be related to the variation of the orbital magnetic moment.

Taking into account that the magnetic signal is contributed by T_d -site Co^{2+} dominantly, we can understand the reduced spin and orbital magnetic moment in the following scenario. For T_d - Co^{2+} with $3d^7$ electronic configuration in the

single-electron picture, the low-lying e_g energy levels ($d_{x^2-y^2}$ and $d_{3z^2-r^2}$ orbital) are fully occupied, and three more electrons reside on the high-lying t_{2g} orbitals (d_{xy} , $d_{xz(yz)}$). The spin magnetic moments in the T_d -site Co^{2+} show the high-spin electronic configuration with $S = 3/2$, which contributes to the magnetic signal dominantly. However, upon protonation, one additional electron is introduced to O_h -site Co^{3+} and drives the Co^{3+} ($S = 0$) to Co^{2+} ($S = 3/2$) transition. The strongest magnetic exchange interaction in the spinel structure is between the corner-sharing T_d and O_h as suggested by the calculations of the exchange constants based on the molecular-field approximation [28]. Therefore, O_h - and T_d -site Co^{2+} with approximately 125° Co-O-Co bonding angle are aligned in an antiparallel manner through O-ion mediated antiferromagnetic superexchange [29,30]. Furthermore, the orbital magnetic moment is reduced due to the decreased anisotropy of electron occupations between in-plane oriented (d_{xy} , $d_{x^2-y^2}$) and out-of-plane oriented ($d_{xz(yz)}$, $d_{3z^2-r^2}$) energy levels, which is related to the charge redistribution due to the extra electron doping as well as the crystal-field effects. The enhanced crystal-field effect is suggested by the larger out-of-plane lattice constant c versus in-plane a ratio, accompanying with a preferred high-spin to low-spin state transition due to the energy competition between the crystal field and the energy gain for spin pairing due to Hund's rule.

Figure 3(b) displayed the normalized XMCD signals for different NCO films. The XMCD signal has only been observed for pristine NCO film. The integrated XAS and the integrated XMCD intensity of pristine NCO film are shown in panels (d) and (f), respectively. The spin and orbital magnetic moments at the Ni-site are $\sim(-0.47 \pm 0.04) \mu_B/\text{Ni}$ and $\sim(0.14 \pm 0.01) \mu_B/\text{Ni}$, respectively, assuming the number of holes as 2.5 (corresponding to $\text{Ni}^{2.5+}$ valence state). Even though the XMCD signal resembles the features of O_h coordinated Ni^{2+} in a high-spin configuration [31], the XMCD signal here cannot be associated with Ni^{2+} with $S = 1$ electronic configuration. The resolved XMCD signal arises from the intermediate $\text{Ni}^{2.5+}$ valence state with unpaired electrons possessing parallel spin alignments.

C. Hall measurements

To confirm the origin of the ferromagnetic response by spin-polarized charge carriers, the AHE has been investigated in NCO pristine and NCO_{int} thin films. The AHE is usually superimposed on the normal Hall effect, and the Hall resistivity ρ_H in ferromagnetic materials can be expressed as $\rho_H = \rho_{\text{OH}} + \rho_{\text{AHE}} = R_0 B + R_s M$, where ρ_{OH} and ρ_{AHE} denote the ordinary Hall effect and the AHE, respectively. R_0 and R_s are the normal and anomalous Hall coefficients, B is the magnetic induction, and M is the magnetization perpendicular to the film plane. The ρ_{AHE} can be extracted from the measured ρ_H versus B curves by subtracting the linear ρ_{OH} term observed at higher magnetic fields (0.5–2 T). Figures 4(a) and 4(b) exhibit the ρ_{AHE} as a function of the magnetic field (B) for pristine NCO and NCO_{int} films at 300 and 2 K, respectively. The ρ_{AHE} shows the square-shaped hysteresis, indicating strong evidence of intrinsic ferromagnetism in the films. The saturated ρ_{AHE} values are comparable for pristine and NCO_{int} , and they decrease slightly at 2 K compared to those at 300 K.

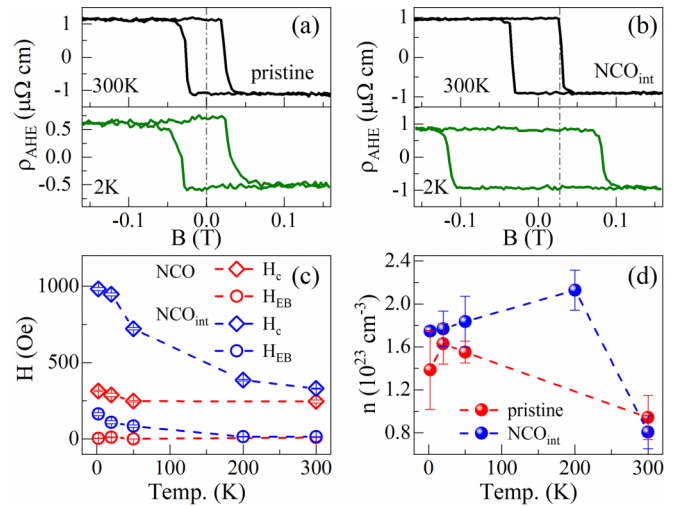


FIG. 4. (a),(b) Magnetic field dependence of the anomalous Hall resistivity ρ_{AHE} for pristine NCO and NCO_{int} thin films measured at 300 and 2 K, respectively. (c) Values of H_{EB} and H_{C} in units of Oe at different temperatures for pristine NCO and NCO_{int} , respectively. (d) Carrier density n as a function of temperatures.

For pristine NCO, the coercivity field (H_{C}) increases slightly from 300 to 2 K, whereas the hysteresis loop remains almost symmetric as shown in Fig. 4(a). Interestingly, the hysteresis loop exhibits a significant shift along the magnetic field axis towards negative field values for NCO_{int} , implying the presence of the exchange-bias effect in NCO_{int} . Accompanying the loop shift, an increased coercivity field H_{C} is also evidenced as the common feature for the exchange-bias effect [32]. Figure 4(c) summarizes the H_{EB} and H_{C} values at different temperatures for pristine NCO and NCO_{int} . The values of the exchange bias (H_{EB}) and H_{C} are defined, respectively, as $H_{\text{EB}} = |H_{+} + H_{-}|/2$ and $H_{\text{C}} = |H_{+} - H_{-}|/2$, where H_{+} and H_{-} are the positive and negative magnetic field values of coercivity as the magnetization goes to zero. For NCO_{int} , both the H_{EB} (~ 15 Oe) and H_{C} (~ 330 Oe) values at 300 K are comparable to those of pristine NCO films at variable temperatures. However, the H_{C} is increased almost three times (~ 985 Oe) and the H_{EB} is approximately 160 Oe at 2 K.

The exchange-bias effect, known as a fundamental magnetic interaction, usually stems from the interfacial exchange coupling between the ferromagnetic and the adjacent antiferromagnetic phases, possessing rich applications such as spin-valve devices and magnetic random access memory, etc. The exchange-bias effect has been observed in a number of ferromagnetic/antiferromagnetic heterostructures, and it can be attributed to the pinned/biased moments and uncompensated spins at the interfaces [33]. Since the exchange-bias effect is absent in pristine NCO with a ferromagnetic ground state, the exchange bias is not related to the antiparallel spin alignments at Ni sites with respect to Co sites. Upon proton doping, the Ni ions are reduced to Ni^{2+} with no magnetic signal as resolved from XMCD spectral analysis at the Ni L_{23} -edge. Meanwhile, the T_d - and O_h -site Co ions exhibit partial valence state reduction. The main magnetic interactions in NCO_{int} are contributed by the ferromagnetic double-exchange interaction between heterovalent Co^{3+} - Co^{2+} states

and the antiferromagnetic superexchange interaction between homovalent Co^{2+} ions at different T_d and O_h sites. Therefore, the exchange-bias effect can be related to the inhomogeneous proton doping where the partial reduction of the magnetic Co sites induces disordered magnetic domains. The partial proton doping gives rise to additional antiferromagnetic phases, which may couple with the incipient ferromagnetic phase and contribute to the exchange-bias effect [34,35]. We further note that the AHE is only contributed by the out-of-plane magnetization. For the XMCD measurements performed here with a tilted angle $\theta = 30^\circ$ as illustrated in the inset of Fig. 3(b), the calculated expectation values of spin magnetic moments obtained by XMCD sum-rule analyses contain both in-plane and out-of-plane contributions, satisfying the following equation: $\langle S^{\theta} \rangle = \langle S^{\theta} \rangle_{\text{in}} * \cos \theta + \langle S^{\theta} \rangle_{\text{out}} * \sin \theta$. Based on the above equation, the different contribution of the expectation values by in-plane and out-of-plane components is not substantial ($\theta = 30^\circ$), which validates the explanation of the exchange-bias effect based on the reduced magnetization at Co sites resolved by XMCD analyses.

Furthermore, the charge carriers can be identified as n -type electrons in pristine NCO and NCO_{int} due to the negative slope of ρ_{OH} at high magnetic field, as expected for the introduction of one extra electron upon proton doping. The R_0 can be used to derive the carrier density n according to the formula $R_0 = -1/ne$, with e as the charge of an electron and n as the carrier density. Figure 4(d) shows the temperature dependence of the carrier density n in pristine NCO and NCO_{int} samples. The n exhibits similar temperature-dependent variations in both samples, where the n is slightly smaller than 1×10^{23} electrons/cm³ at 300 K and increases to $\sim 1.5 \times 10^{23}$ electrons/cm³ at 2 K. The n values are comparable to those resolved in 30 and 10 u.c. NCO films [8]. The comparable values of charge carriers in pristine NCO and NCO_{int} imply that the variation of the energy positions between the conduction-band maximum and the Fermi level is relatively small at the initial state of proton doping.

IV. CONCLUSIONS

Spinel NCO films display the proton concentration-dependent structural, electromagnetic, and electronic structure evolutions. To provide deep insights into the magnetic variations, we performed element-specified XMCD measurements by changing the helicity of the incoming x-ray beam, from which the origins of magnetism in pristine NCO and NCO_{int} as well as the two-proton contained H_2NCO films have been identified. For pristine NCO films, the magnetic dichroism at the Co L_{23} -edge is mainly contributed by the spin magnetic moment in the T_d -site Co^{2+} as well as a minor contribution from T_d -site Co^{3+} . The Ni ions exhibit the preferred intermediate valence state as $\text{Ni}^{2.5+}$ with strong oxygen ligands contribution, and they possess opposite signs of spin arrangements with Co sites.

Upon proton-doping in NCO_{int} films, the magnetic dichroism still exists, which is dominated by T_d -site Co^{2+} . Meanwhile, an additional peak appears that can be assigned to O_h -site Co^{2+} in the high-spin configuration, implying that both T_d - Co^{3+} and O_h - Co^{3+} are reduced to Co^{2+} partially. The magnetic dichroism is absent at the Ni L_{23} -edge for NCO films, indicating a low spin configuration at O_h -site Ni^{2+} . The spin and orbital magnetic moments have also been evaluated quantitatively. NCO_{int} films exhibit a decreased spin magnetic moment, which can be ascribed to the doping of one extra electron that resides at O_h -site Co^{3+} , which changes Co^{3+} ($S = 0$) to Co^{2+} ($S = 3/2$). The O_h -site Co^{2+} aligns in an antiparallel manner with T_d -site Co^{2+} through O-ion mediated antiferromagnetic superexchange interaction. Moreover, the orbital magnetic moment also decreases, which is the reason for the reduced magnetic anisotropy as resolved in MH hysteresis loop compared to pristine NCO films, and it can be related to the charge redistribution of one extra electron doping and the crystal-field effects. In two-proton doped H_2NCO films, the magnetic dichroism is absent where the antiferromagnetism arises from the antiparallel spin alignments of Co^{2+} in T_d and O_h sites.

The origin of ferromagnetic response by spin-polarized carriers has also been evidenced by the AHE. The magnetic-field-dependent ρ_{AHE} shows a square-shaped hysteresis for pristine NCO and NCO_{int} , indicating strong evidence of intrinsic ferromagnetism therein. Interestingly, the NCO_{int} films display an enhanced H_c as well as the exchange-bias effect with an asymmetric hysteresis loop at low temperatures. The exchange-bias effect can be ascribed to the partial Co valence state variation, which gives rise to additional antiferromagnetic phases (superexchange interaction between homovalent Co^{2+} ions at T_d and O_h sites) embedding with the original ferromagnetic phases (double-exchange interaction between heterovalent Co^{3+} and Co^{2+}), as suggested by spin-resolved XMCD analyses. This study provides a fundamental understanding of electric-field controlled magnetization in NCO films for developing spinel-based spintronic applications, and it sheds light on the manipulation of the exchange-bias effect towards spintronic applications of complex oxides via electric-field controlled protonation.

ACKNOWLEDGMENTS

This work was supported by the National Science Foundation of Fujian Province of China (No. 2022J01007), the National Natural Science Foundation of China (Grants No. U22B20132, No. 11972136, and No. 11704317), as well as the Fundamental Research Funds for Central Universities (Grant No. 20720210018). We also acknowledge the beamline scientists at the Magnetic Circular Dichroism beamline (BL12B) of National Synchrotron Radiation Laboratory (NSRL) and the BL08U1-A beamline at Shanghai Synchrotron Radiation Facility (SSRF) for the approval of the beamtime and the kind assistances during the measurements.

[1] U. Bauer, A. J. Tan, P. Agrawal, S. Emori, H. L. Tuller, S. van Dijken, and G. S. D. Beach, *Nat. Mater.* **14**, 174 (2015).

[2] Z. Li, S. Shen, Z. Tian, K. Hwangbo, M. Wang, Y. Wang, F. M. Bartram, L. He, Y. Lyu, Y. Dong, G. Wan, H. Li, N. Lu, J. Zang,

- H. Zhou, E. Arenholz, Q. He, L. Yang, W. Luo, and P. Yu, *Nat. Commun.* **11**, 184 (2020).
- [3] C. Bi, Y. Liu, T. Newhouse-Illige, M. Xu, M. Rosales, J. W. Freeland, O. Mryasov, S. Zhang, S. G. E. te Velthuis, and W. G. Wang, *Phys. Rev. Lett.* **113**, 267202 (2014).
- [4] D. A. Gilbert, J. Olamit, R. K. Dumas, B. J. Kirby, A. J. Grutter, B. B. Maranville, E. Arenholz, J. A. Borchers, and K. Liu, *Nat. Commun.* **7**, 11050 (2016).
- [5] J. Zehner, R. Huhnstock, S. Oswald, U. Wolff, I. Soldatov, A. Ehresmann, K. Nielsch, D. Holzinger, and K. Leistner, *Adv. Electron. Mater.* **5**, 1900296 (2019).
- [6] B. Cui, P. Werner, T. Ma, X. Zhong, Z. Wang, J. M. Taylor, Y. Zhuang, and S. S. P. Parkin, *Nat. Commun.* **9**, 3055 (2018).
- [7] Y. Gu, C. Song, Q. Wang, W. Hu, W. Liu, F. Pan, and Z. Zhang, *APL Mater.* **9**, 040904 (2021).
- [8] X. Chen, X. Zhang, M.-G. Han, L. Zhang, Y. Zhu, X. Xu, and X. Hong, *Adv. Mater.* **31**, 1805260 (2019).
- [9] X. C. Huang, W.-W. Li, S. Zhang, F. E. Oropeza, G. Gorni, V. A. de la Peña O'Shea, T.-L. Lee, M. Wu, L.-S. Wang, D.-C. Qi, L. Qiao, J. Cheng, and K. H. L. Zhang, *Phys. Rev. B* **104**, 125136 (2021).
- [10] M. Wang, X. Sui, Y. Wang, Y.-H. Juan, Y. Lyu, H. Peng, T. Huang, S. Shen, C. Guo, J. Zhang, Z. Li, H.-B. Li, N. Lu, A. T. N'Diaye, E. Arenholz, S. Zhou, Q. He, Y.-H. Chu, W. Duan, and P. Yu, *Adv. Mater.* **31**, 1900458 (2019).
- [11] M. Wu, X. Huang, Y. Li, H. Luo, J. Shi, K. H. L. Zhang, P. Han, S. Hu, T. Deng, Y. Du, L. Chen, H.-Q. Wang, and J. Kang, *Phys. Rev. B* **107**, 125107 (2023).
- [12] C. Wu, W. Guo, C. Zhen, H. Wang, G. Li, L. Ma, and D. Hou, *J. Appl. Phys.* **126**, 043901 (2019).
- [13] X. Chen, Q. Wu, L. Zhang, Y. Hao, M.-G. Han, Y. Zhu, and X. Hong, *Appl. Phys. Lett.* **120**, 242401 (2022).
- [14] D. Kan, L. Xie, and Y. Shimakawa, *Phys. Rev. B* **104**, 134407 (2021).
- [15] X. Xu, C. Mellinger, Z. G. Cheng, X. Chen, and X. Hong, *J. Appl. Phys.* **132**, 020901 (2022).
- [16] P. Silwal, L. Miao, I. Stern, X. Zhou, J. Hu, and D. Ho Kim, *Appl. Phys. Lett.* **100**, 032102 (2012).
- [17] Y. Shen, D. Kan, Z. Tan, Y. Wakabayashi, and Y. Shimakawa, *Phys. Rev. B* **101**, 094412 (2020).
- [18] D. Kan, M. Mizumaki, M. Kitamura, Y. Kotani, Y. Shen, I. Suzuki, K. Horiba, and Y. Shimakawa, *Phys. Rev. B* **101**, 224434 (2020).
- [19] M. Wang, S. Shen, J. Ni, N. Lu, Z. Li, H.-B. Li, S. Yang, T. Chen, J. Guo, Y. Wang, H. Xiang, and P. Yu, *Adv. Mater.* **29**, 1703628 (2017).
- [20] H.-B. Li, F. Lou, Y. Wang, Y. Zhang, Q. Zhang, D. Wu, Z. Li, M. Wang, T. Huang, Y. Lyu, J. Guo, T. Chen, Y. Wu, E. Arenholz, N. Lu, N. Wang, Q. He, L. Gu, J. Zhu, C.-W. Nan *et al.*, *Adv. Sci.* **6**, 1901432 (2019).
- [21] J. F. Marco, J. R. Gancedo, M. Gracia, J. L. Gautier, E. I. Ríos, H. M. Palmer, C. Greaves, and F. J. Berry, *J. Mater. Chem.* **11**, 3087 (2001).
- [22] M. Xue, X. Chen, S. Ding, Z. Liang, Y. Peng, X. Li, L. Zha, W. Yang, J. Han, S. Liu, H. Du, C. Wang, and J. Yang, *ACS Appl. Electron. Mater.* **2**, 3964 (2020).
- [23] Y. Bitla, Y.-Y. Chin, J.-C. Lin, C. N. Van, R. Liu, Y. Zhu, H.-J. Liu, Q. Zhan, H.-J. Lin, C.-T. Chen, Y.-H. Chu, and Q. He, *Sci. Rep.* **5**, 15201 (2015).
- [24] M. Wu, X. Huang, K. H. L. Zhang, S. Hu, L. Chen, H.-Q. Wang, and J. Kang, *Phys. Rev. B* **104**, 075109 (2021).
- [25] R. J. Green, M. W. Haverkort, and G. A. Sawatzky, *Phys. Rev. B* **94**, 195127 (2016).
- [26] K. Fürsich, Y. Lu, D. Betto, M. Bluschke, J. Porras, E. Schierle, R. Ortiz, H. Suzuki, G. Cristiani, G. Logvenov, N. B. Brookes, M. W. Haverkort, M. Le Tacon, E. Benckiser, M. Minola, and B. Keimer, *Phys. Rev. B* **99**, 165124 (2019).
- [27] H. B. Vasili, B. Casals, R. Cicheler, F. Maci, J. Geshev, P. Gargiani, M. Valvidares, J. Herrero-Martin, E. Pellegrin, J. Fontcuberta, and G. Herranz, *Phys. Rev. B* **96**, 014433 (2017).
- [28] C. M. Srivastava, G. Srinivasan, and N. G. Nanadikar, *Phys. Rev. B* **19**, 499 (1979).
- [29] J. Kanamori, *J. Phys. Chem. Solids* **10**, 87 (1959).
- [30] J. B. Goodenough, *Phys. Rev.* **100**, 564 (1955).
- [31] C. Piamonteze, M. Gibert, J. Heidler, J. Dreiser, S. Rusponi, H. Brune, J.-M. Triscone, F. Nolting, and U. Staub, *Phys. Rev. B* **92**, 014426 (2015).
- [32] J. Nogués, J. Sort, V. Langlais, V. Skumryev, S. Suriñach, J. Muñoz, and M. Baró, *Phys. Rep.* **422**, 65 (2005).
- [33] X. W. Wu and C. L. Chien, *Phys. Rev. Lett.* **81**, 2795 (1998).
- [34] M. Gu, Q. Xie, X. Shen, R. Xie, J. Wang, G. Tang, D. Wu, G. P. Zhang, and X. S. Wu, *Phys. Rev. Lett.* **109**, 157003 (2012).
- [35] C. Wang, C. Chen, C.-H. Chang, H.-S. Tsai, P. Pandey, C. Xu, R. Böttger, D. Chen, Y.-J. Zeng, X. Gao, M. Helm, and S. Zhou, *ACS Appl. Mater. Interfaces* **10**, 27472 (2018).